May 1, 2000

Optical remote sensing of the thermosphere with heater induced artificial airglow (HIAA)

P. A. Bernhardt
M. Wong
J. D. Huba
Bela G. Fejer, *Utah State University*
L. S. Wagner, et al.

JOURNAL OF GEOPHYSICAL RESEARCH, VOL. 105, NO. A5, PAGES 10,657–10,671, MAY 1, 2000

Optical remote sensing of the thermosphere with HF pumped artificial airglow

P. A. Bernhardt,[1] M. Wong,[1,2] J. D. Huba,[1] B. G. Fejer,[3] L. S. Wagner,[4] J. A. Goldstein,[4,5] C. A. Selcher,[4] V. L. Frolov,[6] and E. N. Sergeev[6]

Abstract. Optical emissions excited by high-power radio waves in the ionosphere can be used to measure a wide variety of parameters in the thermosphere. Powerful high-frequency (HF) radio waves produce energetic electrons in the region where the waves reflect in the *F* region. These hot or suprathermal electrons collide with atomic oxygen atoms to produce localized regions of metastable $O(^1D)$ and $O(^1S)$ atoms. These metastables subsequently radiate 630.0 and 557.7 nm, respectively, to produce clouds of HF pumped artificial airglow (HPAA). The shapes of the HPAA clouds are determined by the structure of large-scale ($\approx$10 km) plasma irregularities that occur naturally or that develop during ionospheric heating. When the HF wave is operated continuously, the motion of the airglow clouds follows the $\mathbf{E} \times \mathbf{B}$ drift of the plasma. When the HF wave is turned off, the airglow clouds decay by collisional quenching and radiation, expand by neutral diffusion, and drift in response to neutral winds. Images of HPAA clouds, obtained using both continuous and stepped radio wave transmissions, are processed to yield the electric fields, neutral wind vectors, and diffusion coefficients in the upper atmosphere. This technique is illustrated using data that were obtained in March 1993 and 1995 at the ionospheric modification facility near Nizhny Novgorod, Russia. Analysis of HPAA clouds yields zonal plasma drifts of 70 m s^{-1} eastward at night. On the basis of artificial airglow from energetic electrons generated at 260 km the zonal neutral wind speed was estimated to be 96 m s^{-1} and the $O(^1D)$ diffusion coefficient was determined to be between 0.8 and 1.4 $\times$ 10^{11} cm^2 s^{-1}. The quenched lifetime of the $O(^1D)$ was determined to be 29.4 s. The diffusion and quenching rates are directly related to the atomic and molecular concentrations in the thermosphere. Improvements in the remote-sensing technique may be obtained if the intensity of the artificial airglow emissions is increased. High-power radio transmissions employing pulse sequences and tuning near electron cyclotron harmonics were attempted to increase the optical emissions. Both of these, however, produced reduced intensity, and consequently, continuous transmission at frequencies away from electron gyro harmonics is the preferred heating regime.

1. Introduction

Improvements and validation of complex models of the upper atmosphere require measurements of composition, winds, and temperatures for both the ionized and neutral constituents. Databases of these parameters have been obtained using a variety of techniques with both ground-based and in situ satellite or rocket-based instruments. The ground-based measurements have used Fabry-Perot interferometers and incoherent scatter radars. In space, ion mass spectrometers, extreme ultraviolet spectrometers, and chemical release tracers have been employed. This paper outlines the use of optical emissions produced artificially by high-power radio waves for determining many properties of the upper atmosphere.

High-power radio waves that impinge on the ionosphere can produce plasma irregularities and enhanced optical emissions that can be employed for remote sensing of the upper atmosphere. Artificial plasma structures take the form of (1) large-scale ($\approx$10 km) cavities driven by bulk plasma heating and self-focusing [*Hansen et al.*, 1992], (2) small-scale field-aligned irregularities ($\approx$10–100 m) produced by ponderomotive or thermal pressure [*Bernhardt et al.*, 1995; *Kelley et al.*, 1995; *Gurevich et al.*, 1998], or (3) quasi-horizontal stratifications produced by the standing wave of the high-power radio transmission [*Belikovich et al.*, 1975]. Artificial airglow enhancements occur when the plasma electrons become hot enough or energetic enough to excite background neutral species by inelastic collisions. The greatest electron heating or acceleration occurs in regions where the HF waves are focused by plasma irregularities. Consequently, the presence of enhanced airglow is tied closely to both natural and artificial irregularities in the ionosphere.

Artificial ionospheric irregularities and airglow clouds can be used as tracers to study portions of the upper atmosphere and ionosphere. Both radio and optical techniques have been

[1]Beam Physics Branch, Plasma Physics Division, Naval Research Laboratory, Washington, D. C.
[2]Now at Department of Physics, Carnegie Mellon University, Pittsburgh, Pennsylvania.
[3]Center for Atmospheric and Space Sciences, Utah State University, Logan.
[4]Information Technology Division, Naval Research Laboratory, Washington, D. C.
[5]Now at Scientific and Engineering Solutions, Annapolis Junction, Maryland.
[6]Radiophysical Research Institute, Nizhny Novgorod, Russia.

Paper number 1999JA000366.
0148-0227/00/1999JA000366$09.00

used to detect the motion of these tracers to yield drift velocities for the plasma and neutral atmosphere. The echoes from artificial periodic irregularities result from Bragg scatter by HF pulses. Doppler shifts in the scattered pulses have provided the vertical drift information [*Belikovich et al.*, 1975; *Rietveld et al.*, 1996; *Djuth et al.*, 1997]. The motion of artificial airglow clouds linked to plasma irregularities has been used to determine the horizontal drift of the F layer plasma [*Bernhardt et al.*, 1989a].

Following the termination of the high-power radio source, the artificial ionospheric disturbances dissipate. The decay of plasma irregularities provides a measure of plasma diffusion in the upper atmosphere. Using this technique, the collisional diffusion rate in the mesosphere and lower thermosphere has been estimated [*Belikovich et al.*, 1975]. During ionospheric heating experiments the artificial airglow clouds decay and expand after the electromagnetic wave source is removed. Neutral diffusion and collisional quenching in the upper atmosphere control the evolution of artificial airglow after heater turnoff.

In this paper, measurements of artificial airglow produced by high-power radio waves are employed to determine properties of the upper atmosphere. Section 2 reviews previous experimental and theoretical work on artificial airglow production and decay. Section 3 describes the experimental measurements of enhanced 630 nm emissions made using the Russian HF facility called "SURA." Section 4 is an overview of the airglow measurements. Section 5 deals with analysis for continuous heating experiments. Here plasma drifts obtained from observations of the motion of artificial airglow clouds are compared with the expected $\mathbf{E} \times \mathbf{B}$ drifts over the HF facility. Analysis of the optical emissions following heater turnoff is discussed in Section 6. The horizontal neutral winds and diffusion coefficients are determined from the decay and expansion of the airglow clouds. Section 7 contains a comparison of the measured quantities with models of the upper atmosphere composition and winds. Improvements in the experimental techniques are suggested in section 8.

2. Previous Work

The first reported measurements of enhanced airglow from high-power radio waves occurred in 1970 using the high-power HF facility at Platteville, Colorado [*Utlaut and Cohen*, 1971]. Subsequently, the excitation of airglow by high-power radio waves has been observed with photometers located at Arecibo, Puerto Rico [*Sipler and Biondi*, 1972; *Carlson et al.*, 1982; *Fejer et al.*, 1985; *Bernhardt et al.*, 1988a, 1989b]; at Platteville, Colorado [*Haslet and Megill*, 1974]; at Moscow, Russia [*Adieshvili et al.*, 1978]; and at Tromsö, Norway [*Stubbe et al.*, 1982; *Henriksen et al.*, 1984]. *Sergienko et al.* [1997] report modulation of the auroral green line intensities by ionospheric heating at Tromsö.

The first images of the artificially enhanced red line (630 nm) or green line (577.7 nm) were reported by *Moore* [1983] using the Platteville heating facility. Images of 630 nm emissions have been readily obtained using intensified CCD imagers at Puerto Rico [*Bernhardt et al.*, 1988a, b, 1989a, b], at the SURA heating facility in Russia [*Bernhardt et al.*, 1991], and the European Incoherent Scatter (EISCAT) HF facility in Tromsö [*Brändström et al.*, 1999].

Much of the research in artificial airglow from HF facilities has dealt with the production of the emissions. Both thermal and suprathermal processes have been considered. *Mantas* [1994] and *Mantas and Carlson* [1996] have shown that bulk heating of the plasma can produce electron temperatures (2000–4000 K) that are large enough to excite the red line of atomic oxygen. Several authors [*Haslet and Megill*, 1974; *Bernhardt et al.*, 1989b] have maintained that suprathermal electron distributions are required to explain the green line emissions observed by a number of experimenters [*Moore*, 1983; *Fejer et al.*, 1985; *Bernhardt et al.*, 1989b]. *Wang et al.* [1997] have modeled the production of suprathermal tails in the electron distribution. It is likely that both thermal and suprathermal electron distributions contribute to the excitation of atomic oxygen by electron collisions.

Another aspect of HF pumped artificial airglow (HPAA) is remote sensing of the upper atmosphere. *Sipler and Biondi* [1972] estimated the quenching of $O(^1D)$ by reactions with O_2 and N_2 by observing the build up and decay of HPAA as the heating facility was cycled on and off. *Bernhardt et al.* [1989b] demonstrated that plasma drifts in the F region could be measured by observing the motion of the HPAA clouds. The airglow clouds are linked to drifting plasma irregularities that focus the high-power radio waves near the reflection level in the ionosphere. The enhanced electric fields in the focus regions produce larger energetic electron fluxes and consequently more intense optical emissions from these regions. Comparing the plasma velocities obtained from the drifting airglow clouds with those obtained using the Arecibo incoherent scatter radar validated the technique.

In the F region above 200 km altitude the primary species excited by high-power radio waves is atomic oxygen. The $O(^1D)$ state has a lifetime of ~1 min depending on the quenching by collisions with ambient species. At the SURA facility in Russia the 630 nm emission from the $O(^1D)$ is bright enough to be recorded with ground-based low-light-level imaging systems. As far as we know, the higher-energy $O(^1S)$ state and its characteristic 557.7 nm emissions have never been detected at SURA.

3. Experiment Description

A diagram of the optical observations for the ionospheric modification experiment is shown in Figure 1. Imaging systems are set up near the radio wave transmitter to view the night sky. The full field of view was selected to capture the 8°-wide HF beam as well as any expansions of motions of the artificial airglow.

A collection of computer-controlled, low-light-level imaging instruments were set up by the Naval Research Laboratory at the SURA heating facility near Vasil'sursk, Russia (56.13°N latitude, 46.10°E longitude). The magnetic dip angle at SURA is 71°. The instrumentation consisted of (1) an intensified CCD camera with a 512 × 512 detector array for slow scan imaging, (2) an intensified CCD camera with a 768 × 493 pixel array operating at 60 Hz scan rates, and (3) a photometer with a Si microchannel plate (MCP) detector.

The intensified slow scan imager was used to record 10 Rayleigh or greater enhancements in the 630 nm airglow over SURA by using 45 s integration times, digitizing the CCD array pixels with 12 bit resolution, and storing the data in computer memory. The CCD array was thermoelectrically cooled to −30°C. This camera was a Photometrics IC200 with a Series 200 Camera Controller. An ITT F4113 MCP intensifier with a 40 mm diameter S-20 photocathode was used as a camera shutter as well as providing photon gain. A Keo telecentric

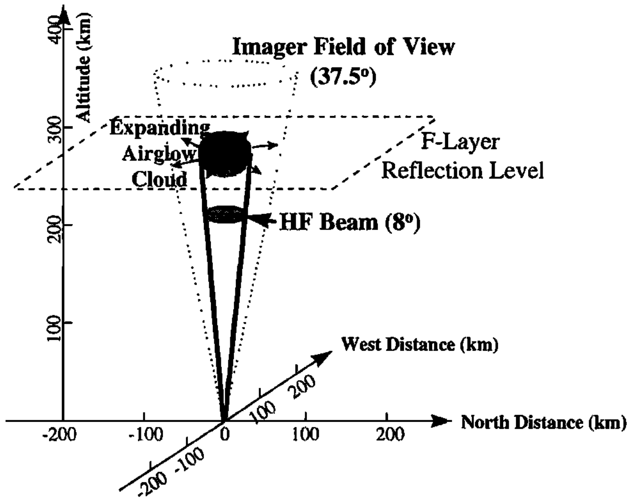

Figure 1. Optical observation geometry for the 1993 and 1995 SURA campaigns. The CCD imager field of view was chosen to capture motion and expansion of the 630 nm airglow cloud. The HF radio beam is typically 8°. The size of the artificial airglow cloud will be affected by field-aligned irregularities near the HF wave reflection altitude, transport of the energetic electrons, and diffusion of the radiating species.

optical system provided a 50° field of view of the night sky with light passing through the 3 nm passband of a 630 nm interference filter. The exact field of view (36.5°) and observation direction of the camera was determined from the star field, which is recorded in each airglow image. The CCD array had a 512 × 512 pixel format, and at 250 km altitude the image resolution was 361 m/pixel. The camera was calibrated at the site using a portable fluorescent source that had a radiance of 895 R/nm at a wavelength of 630 nm.

A second intensified CCD camera was operated at video rates of 30 frames s^{-1} to monitor the night sky for clouds. The camera was a Xybion Model ISG-250 with an extended red photocathode on the intensifier. This camera was operated without a filter. This type of cloud monitor is important to ensure that fluctuations in the red line intensity are due to ionospheric and not tropospheric processes.

In addition to imaging, it is useful to have a photometer to monitor the total intensity over a part of the night sky. The photometer provides more sensitivity and higher temporal response than an imaging system. The detector in the photometer was an ITT F4149 MCP photomultiplier with an S-20 extended red photocathode. This detector is housed in a Peltier chamber for cooling to −30°C. Individual counts from the detector anode are accumulated and stored once every 100 ms. Both 630 and 557.7 nm filters were placed in front of the optical entrance to the photometer.

The artificial airglow in the upper atmosphere was excited using the three transmitters that compose the SURA HF facility. Each transmitter provided 250 kW continuous power over a tuning range of 4.3 and 10 MHz. The HF frequencies were determined with computer-controlled frequency synthesizers. The output of each transmitter was connected to a separate 4 × 12 phased array of wideband dipoles. The three sections together composed a 12 × 12 array antenna that was 300 m on each side. The full antenna beam is 8° × 8° at 5.75 MHz. Phasing of the three transmitters permitted steering of the HF beam by ±40° from the zenith in the north-south direction. The measured gain of the antenna array is frequency-dependent, varying from 200 at 4.8 MHz to 380 at 9.3 MHz. Both steering and power control are provided at the transmitter site. Rapid beam swinging of ±8° is possible with electronic steering. Changes in mechanical linkages are required for larger deviations in beam angle up to 40° from zenith. By controlling the transmitter power and the HF beam location, excitation thresholds and zenith angle effects on the intensities of artificial airglow were studied.

A previous artificial airglow campaign occurred at SURA in September 1990. *Bernhardt et al.* [1991] described the results of this campaign. The SURA observations of enhanced airglow reported here occurred during the periods of March 13–22, 1993, and March 21 to April 4, 1995. Both stimulated electromagnetic emission (SEE) and artificial airglow experiments were conducted during that time period. *Bernhardt et al.* [1994] reported the results of the 1993 SEE experiments. The 1995 SEE experiments are described by *Wagner et al.* [1999]. All three papers provide additional details on the diagnostic and modification capabilities at the SURA facility.

The measurement of optical emissions by high-power radio wave from the ground is limited by (1) obstruction by tropospheric cloud cover, (2) sunlight or moonlight interference, and (3) decay of the critical frequency of the *F* region after sunset. The lowest operational frequency for the SURA facility is 4.3 MHz. Often, the *F* region is only dense enough to reflect the heater frequencies for a few hours after sunset. Consequently, the artificial airglow studies were only conducted for a small fraction of the total experimental time available. Table 1 lists the periods of time when airglow measurements were made at SURA in 1993 and 1995. The local time at SURA is 3 hours later than the Universal Time given in Table 1.

4. Optical Observations

This section contains examples of the red line (630 nm) optical data acquired during the ionospheric modification campaigns at SURA in 1993 and 1995. The data show the effects of transitions between overdense and underdense heating, plasma drifts, transmitter antenna tuning, neutral diffusion and winds, pump power variations, and variations in the antenna

Table 1. Schedule of Optical Measurements at SURA

Date	Time, UT	Frequencies, MHz	Primary Purpose
March 21, 1993	1610–2000	5.8288, 4.785, 4.300	airglow drifts
March 24, 1995	1632–1900	4.786, 4.300	power threshold
March 25, 1995	1700–1840	4.300	pulse duty cycle
April 3, 1995	1720–1911	4.595	continuous wave heating
April 4, 1995	1700–1800	4.300	beam swinging

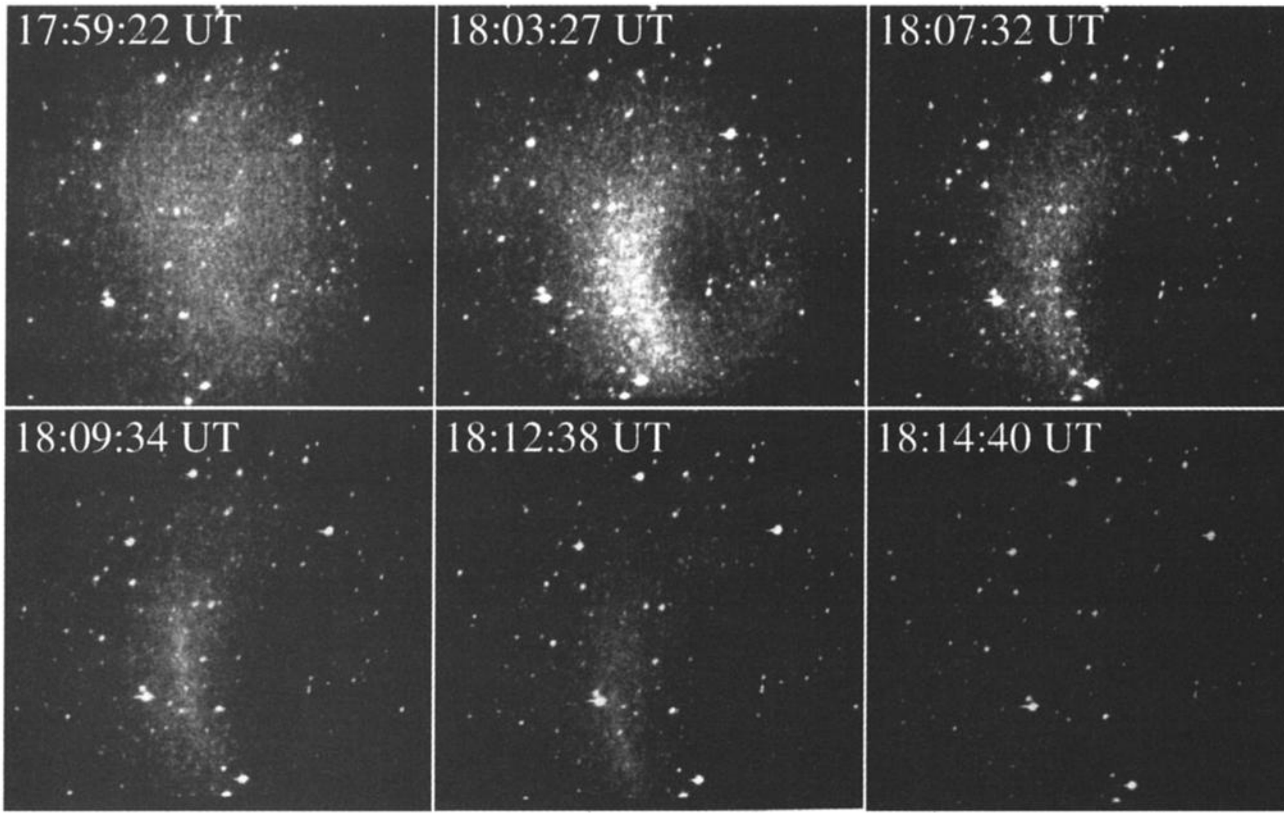

Figure 2. Decay of the ionosphere on March 21, 1993, causing a transition from overdense to underdense heating. The 5.8288 MHz wave is beamed continuously to the ionosphere. Each 630 nm image is an 85 × 85 km sample of the airglow at the zenith of the HF facility in the night sky. West is to the right, and north is at the top of each frame. A crescent of airglow is formed around the region of the layer that has been penetrated by the HF beam. The airglow intensity increases by a factor of 2 in the crescent before decaying completely. This intensification may be due to acceleration along a larger distance in the layer at the edge of the penetration region.

position. All of the 630 nm images have north to the top and west to the right of the frames.

The objective of some tests at SURA were to enhance the artificial airglow intensities. It is important to produce the brightest airglow to improve the quality of the remote-sensing measurements. The most intense airglow is produced by (1) using an HF that is slightly less than the critical frequency of the layer, (2) providing the largest equivalent radiated power (ERP) to the plasma, and (3) using ordinary (as opposed to extraordinary) mode transmissions. The transmission frequency is selected to be the largest that reflects in the ionosphere. The transmitters are tuned to maximum efficiency, and the antenna array is properly phased to produce a well-collimated radio wave beam with the proper polarization. Unsuccessful attempts were made to produce greater airglow intensities by (1) pulsing the transmissions and (2) tuning to harmonics of the electron gyrofrequency in the ionosphere.

After sunset the ionospheric densities over SURA decay, and the critical frequency can make a transition from being larger than the pump frequency (i.e., overdense) to being less than the pump frequency (i.e., underdense). During this transition period, part of the ionosphere may be overdense, and a different region may be underdense. The energetic electrons responsible for airglow are thought to be from just below the overdense regions of the ionosphere where the reflected electromagnetic waves are converted into Langmuir waves with accelerate electrons to suprathermal velocities [*Bernhardt et al.*, 1989b; *Wang et al.*, 1997] or where substantial electron heating occurs [*Mantas*, 1994; *Mantas and Carlson*, 1996; *Gurevich and Milikh*, 1997].

A sequence of images of the artificial airglow during the transition periods when the layer goes from overdense to underdense is illustrated in Figure 2 for March 21, 1993. The HF pump frequency was 5.8288 MHz. At 1759 UT the airglow cloud is diffuse with a peak intensity of 30 R. Four minutes later the peak intensity has increased to 50 R on the left (east) side of the cloud. By 1807 UT the airglow cloud has formed into a crescent next to a region where the airglow intensities have been reduced to ambient levels. This cloud finally vanishes by 1814 UT. The dark region in the airglow images from 1803 to 1810 UT may identify regions where the HF wave has penetrated the F region to form an underdense hole near the zenith of the HF facility. The brightness at the side of the hole is thought to be due to increased interaction distances for electron acceleration. The edge of this hole remains overdense for ~10 min until ion-electron recombination acts to reduce the maximum density below the critical density needed for reflection.

After the ionosphere became underdense for 5.8288 MHz, the pump frequency was reduced to 4.785 MHz and, when that frequency became underdense, to 4.3 MHz. For the next 30

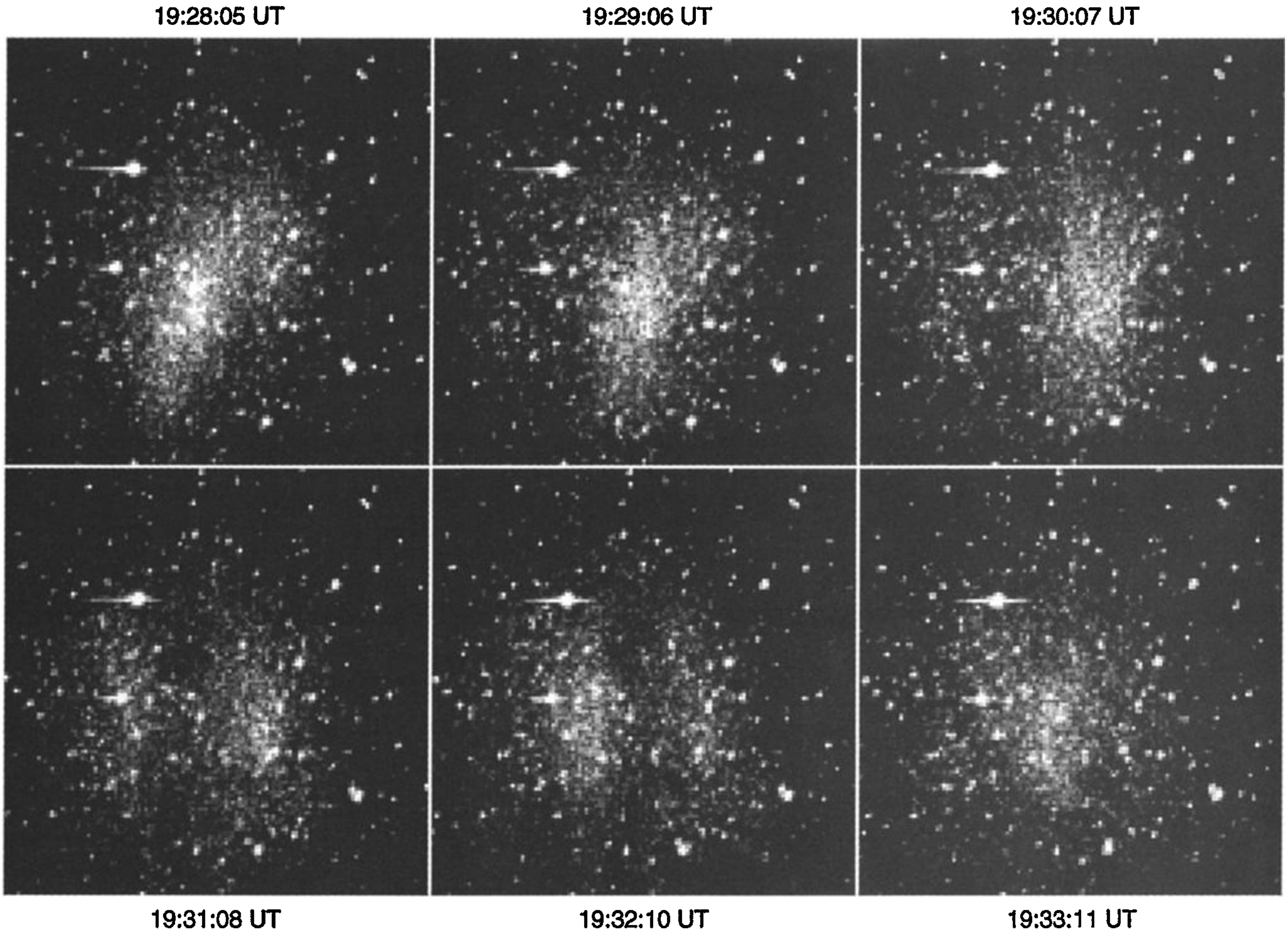

Figure 3. Motion of an artificial 630 nm airglow cloud across the night sky on March 21, 1993, excited by 4.3 MHz. After the cloud drifts to the edge of the HF beam it disappears, and another cloud appears at the opposite edge. This cloud motion is produced by electric fields in the *F* region.

min, continuous measurements were obtained showing convection of the artificial airglow clouds.

Often the airglow clouds seem to move in the zonal (east-west) direction above the heating facility. As a cloud drifts away from the zenith of the transmitter antenna, it becomes weaker, disappears, and then is eventually replaced by a new cloud. A sample of this effect is illustrated in Figure 3 for March 21, 1993. At this time the HF facility was operating at 4.3 MHz with ~150 MW ERP. The time between successive images is ~1 min, and the image field of view is 85 × 85 km. This motion is due to refraction of the top of the radio beam by large-scale density depressions that follow the ambient plasma drift. These *F* region, bottomside depressions may be generated by the heater beam or may occur naturally. Estimation of the horizontal plasma drift from the motion of the airglow clouds is described in section 5.

One use for observations of artificial optical emissions is checking the antenna pattern of HF heating facilities. When the transmission frequency is changed by >50 kHz at SURA, the phased antenna array must be adjusted. During the rephasing process the output signals for two of the transmitters are adjusted with respect to a third reference transmitter. Optical measurements were made while rephasing was occurring for full power on all three transmitters. This is illustrated in Figure 4 for March 24, 1995. The transmitters had been operating at 5.100 MHz, and the transmission frequency was changed to 4.786 MHz. After the frequency change at 1712 UT the beam remained well focused but was tilted to a region 12° to the north of zenith. Between 1713 and 1715 UT the radio beam was reformed to change the pointing direction. At 1716 UT the 4.786 MHz radio beam was adjusted to the zenith of the heating facility.

The excitation of artificial airglow often appears at a threshold of RF power [*Bernhardt et al.*, 1989b]. Figure 5 illustrates the airglow images for power levels of 10 MW (−10 dB), 32 MW (−5 dB), and 100 MW (0 dB) of transmitter power at 4.3 MHz. These data were taken between 1822 and 1828 UT on March 24, 1995, when the ionospheric densities were stable, as measured by the SURA ionosonde. For these particular images the airglow intensity rises sharply from 5 to 45 R for transmitter power changes from 10 to 32 MW. A further increase in power to 100 MW only produces a slight (50 R) increase in intensity above the background.

For remote sensing applications it is important to generate the largest possible intensity of HPAA. Along with providing the maximum power into a well-phased antenna, there may be some other techniques to increase the airglow intensity. Temporal variations in HF power, which can yield enhancements in SEE [*Wagner et al.*, 1999], may also enhance the efficiency of electron acceleration. Tests were conducted to determine if

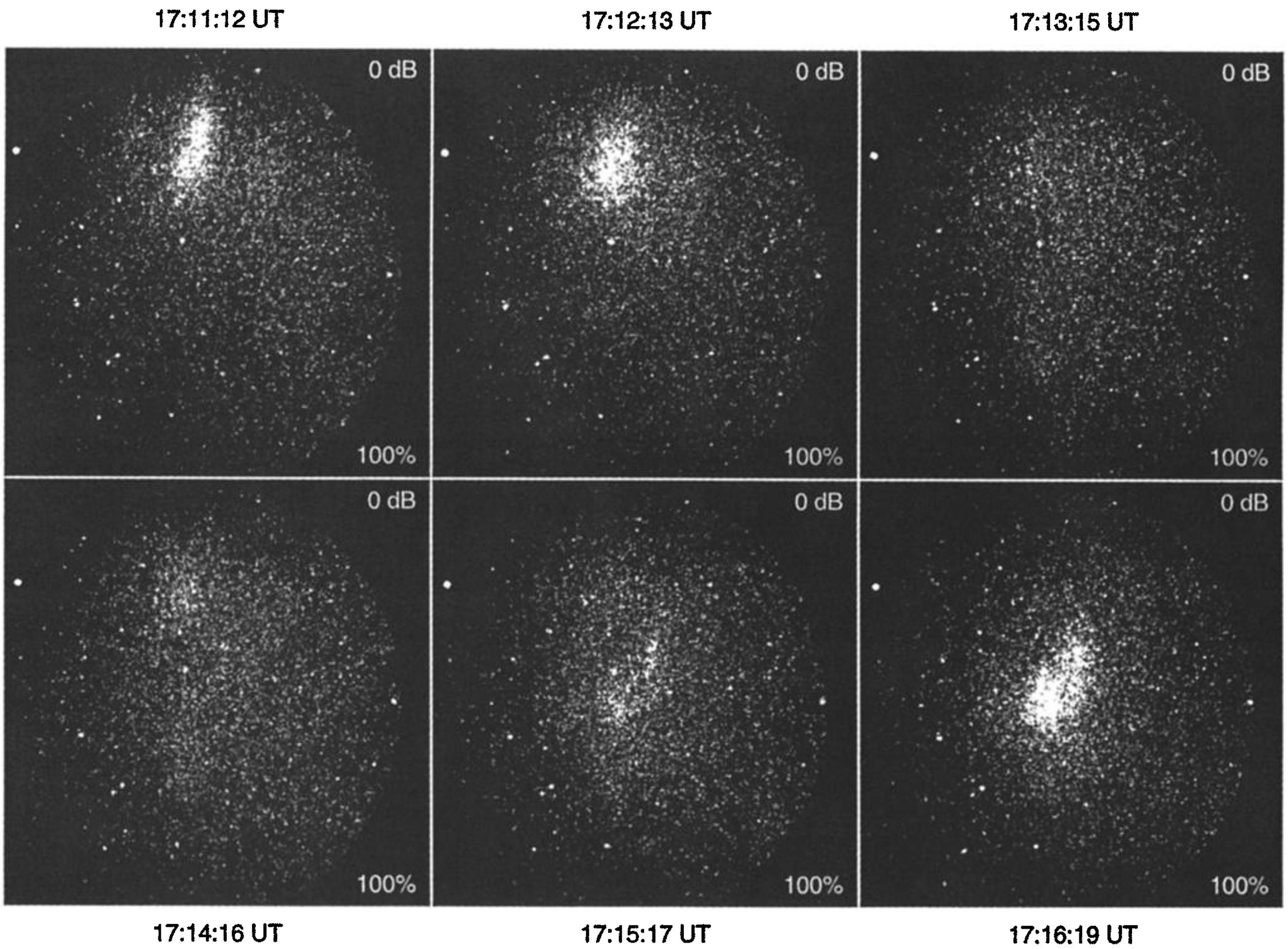

Figure 4. Dynamic reforming of the HF beam on March 24, 1995, from 12° north of zenith to the zenith of the HF facility. The HF transmissions at 4.786 MHz were maintained at full power during this operation.

pulsing the HF transmission would lead to enhanced optical emissions. On March 25, 1995, the average power from the HF facility was changed both by varying the attenuation for continuous wave transmissions and by changing the duty cycle for pulsed transmissions at full peak power. Each pulse cycle had a period of 2 s. A 50% duty cycle employed sequences of 1 s on and 1 s off. The 75% duty cycles had 1.5/0.5 s on/off sequences. For comparison, transmitter attenuation was used to yield the same average power for continuous transmissions. Reducing the power by half either with (−3 dB) attenuation or with 50% duty cycles produced the identical effect on the airglow intensities. At half the full transmitter (on 4.3 MHz) the airglow intensities were reduced to a few rayleighs above the background. Increasing the duty cycle to 75% yielded ~30 R peak intensity, and a duty cycle of 100% or 0 dB attenuation increased the red line enhancement to 40 R. These measurements were made from 1730 to 1830 UT, and no nonlinear effects of pulsed transmissions on airglow intensity were recorded.

Finally, it is well known that high-power radio waves show different effects when the waves are tuned to harmonics of the electron gyrofrequency [*Leyser et al.*, 1989; *Stubbe et al.*, 1994; *Stubbe*, 1996]. SEE and anomalous absorption (AA) have been shown to change characteristics near the third, fourth, and fifth harmonics of the electron gyrofrequency, $\Omega_e \cong 2\pi$ 1.32 MHz, in the *F* region. When the HF wave is tuned to a gyro harmonic, both the SEE and AA are minimized. Certain SEE "gyro features" such as the broad upshifted maximum (BUM), downshifted peak (DP), and broad symmetrical structure (BSS) only appear for HF transmissions near the gyro harmonics. Other "universal features" such as the continuum and downshifted maximum (DM) SEE spectra and AA only exist away from the gyro harmonic transmissions for the HF facilities. The changes in these features are attributed to striation formation [*Stubbe*, 1996] and to interactions with electron Bernstein waves [*Huang and Kuo*, 1994; *Hussein et al.*, 1998].

Electron acceleration and subsequent airglow production should also be strongly affected by the proximity of the HF pump frequency to a gyro harmonic. Preliminary experiments were carried out at SURA to determine if transmitting powerful waves near electron gyro harmonics has any effect on airglow intensity. Gyro harmonic heating occurred on March 24 at 1632 UT with 5.105 MHz, on March 25 at 1640 UT with 5.180 MHz, and on March 26 at 1222 UT with 5.202 MHz. All 3 days showed the SEE features BUM, DP, and DM for pump frequencies near the fourth ($n = 4$) gyro harmonic [*Wagner et al.*, 1999]. In all cases the 630.0 nm airglow vanished for the gyro harmonic transmissions of powerful HF waves. This indicates that electron acceleration is inhibited near the fourth harmonic. Further work needs to be done in this area concern-

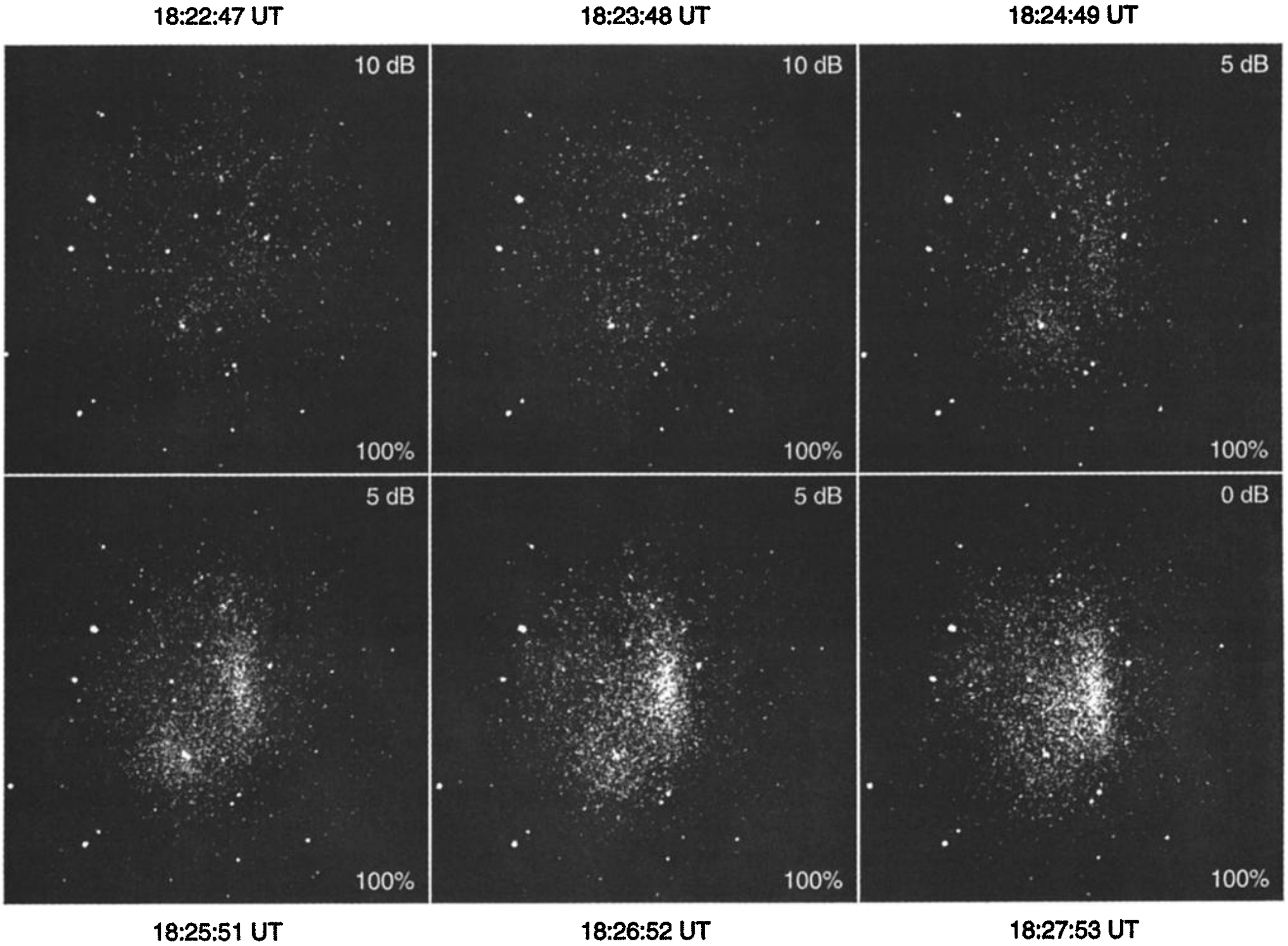

Figure 5. Sequence of 630 nm airglow images showing the effects changing the 4.3 MHz transmitter power. The attenuation was set at 10, 5, and 0 dB, as given in the top right corner of each image. The transmitter duty cycle was 100%. The airglow threshold is found for between 10 and 5 dB attenuation of the transmitter power.

ing the frequency range around the third, fourth, and fifth harmonics over which airglow emissions are not produced. This is a difficult experiment at SURA because the ionosphere is continuously decaying after sunset, the reflection altitude rises, and the tuning to the electron gyro harmonics is constantly changing.

5. Plasma Drift Determination

By simultaneous comparison with incoherent scatter radar (ISR) drift measurements it has been established that artificial airglow clouds move at the plasma drift velocity [*Bernhardt et al.*, 1989a]. Electric fields in the ionosphere move the bulk plasma at a velocity given by $\mathbf{V} = \mathbf{E} \times \mathbf{B}/B^2$. Both natural and heater-induced irregularities near the HF reflection height drift at this velocity across the radio frequency beam. Focusing of the HF waves in the underdense sections of the irregularities increases the power density of the pump wave. The focusing yields enhanced heating, larger fluxes of energetic electrons, and higher airglow intensities. Thus the airglow clouds follow the motion of the large-scale (>4 km) irregularities that pass through the HF beam near reflection.

The first step in processing the airglow images to determine plasma drifts is to remove stars and noise with a 5×5 pixel median filter [*Bracewell*, 1995]. This filter replaces the intensity of the 25 pixel block by its median value. A median filter preserves sharp edges while suppressing noise in pixels as well as eliminating point sources such as stars. The star removal is important so that the star motion does not contaminate the airglow cloud motion in the image. Figure 6 shows an example of a filtered image by processing the data used for Figure 3. All of the image processing uses 512×512 arrays of pixels holding images collected using a $t_0 = 45$ s integration time with $\Delta t = 61$ s between successive exposures.

The vector horizontal displacement between successive images is obtained with a cross-correlation analysis. Consider an image described by an intensity function $S_i(x, y)$ at time t_i, where x and y are the spatial coordinates projected from the image plane of the camera onto the sky. The cross-correlation function is given by

$$C_{ij}(\alpha, \beta) = \int_{-\infty}^{\infty} \int_{-\infty}^{\infty} S_i(x, y) S_j(x + \alpha, y + \beta)\, dx\, dy, \tag{1}$$

where (α, β) are the shifts of image i from image j in the east and north directions, respectively. The integrals in (1) act as a filter to produce a smooth result.

The maximum of the cross-correlation function provides the cloud displacement between images. The maximum of $C_{ij}(\alpha_{\max}, \beta_{\max})$ is found numerically. The horizontal drift vec-

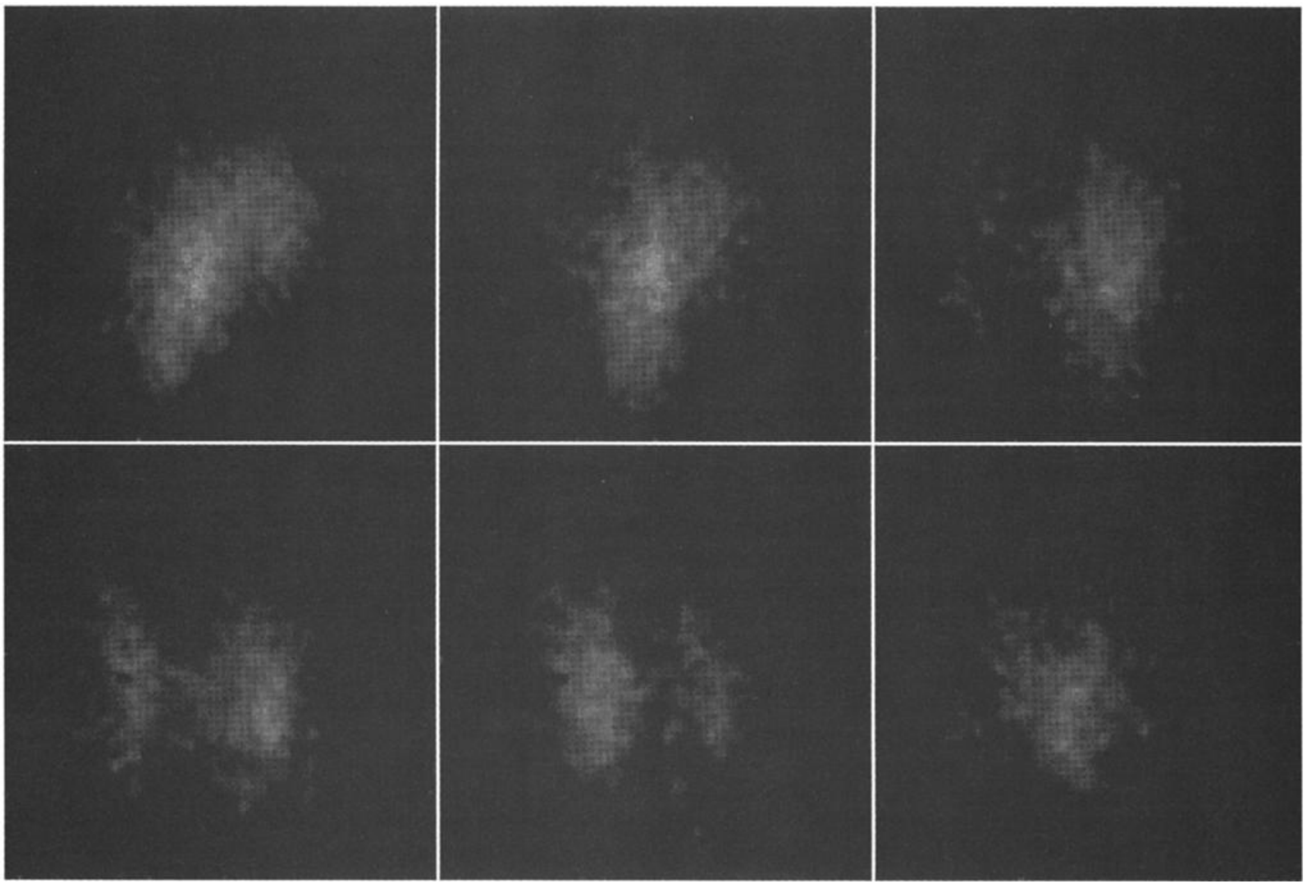

Figure 6. Filtered images of 630 nm emissions excited by 4.3 MHz on March 21, 1993. A median filter is used to remove stars and noise speckles while preserving the shape of the airglow clouds. The filtered image is used to obtain plasma drifts.

tor at time $t = (t_i + t_j)/2$ is $\mathbf{V}_X(t) = \alpha_{max}/(t_j - t_i)$ and $\mathbf{V}_Y(t) = \beta_{max}/(t_j - t_i)$. The cross correlation for the two images at 1929:06 and 1930:07 UT of Figure 6 is illustrated in Figure 7. The maximum is found at $(\alpha_{max}/\Delta t,\ \beta_{max}/\Delta t) = (76.0, 3.2)$ m s^{-1}, where $\Delta t = 61$ s, the time between images. The width of the cross-correlation function indicates that the uncertainties of the drift measurements are ~15 m s^{-1} in the zonal direction and 30 m s^{-1} in the meridional direction.

This cross-correlation analysis was performed on all of the images obtained between 1927 and 1937 UT on March 21, 1993, at SURA. The resulting drifts are shown by Figure 8. The plasma drift component in the zonal, eastward direction is found to be relatively constant with a value between 60 and 76 m s^{-1} over the 10 min span of time except for a sudden acceleration to between 110 and 120 m s^{-1} near 1933 UT. The northward velocity based on the cross-correlation analysis varies between -25 and 3 m s^{-1} with an average of -9.5 m s^{-1}. For validation of these values obtained at 56.13°N latitude a comparison is made with those obtained using an ISR located in the European region at similar latitudes. The zonal plasma convection of 68 ± 8 m s^{-1} is within the range for equinox values of the east-west component of 35–95 m s^{-1} obtained at 44.65°N latitude at the Saint-Santin incoherent scatter radar in

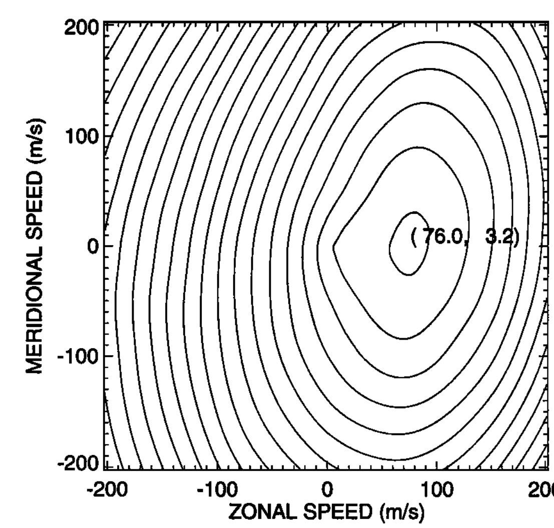

Figure 7. Cross correlation of the second and third images of Figure 6, obtained on March 21, 1993. Velocities are obtained by scaling the cross correlation with the time between images. The peak of the cross-correlation function indicates that the airglow clouds are moving at 76.0 m/s in the zonal direction and 3.2 m/s in the meridional direction.

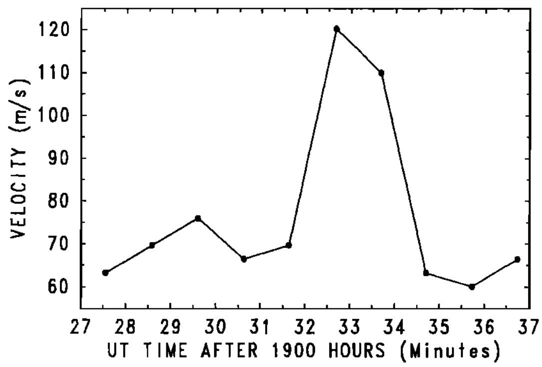

Figure 8. Zonal plasma drifts obtained using the series of airglow clouds obtained between 1927 and 1937 UT on March 21, 1993, at SURA. The average zonal speed is 68 m/s with a burst of acceleration to 115 m/s for 2 min.

France [*Blanc et al.*, 1977; *Blanc and Amayenc*, 1979]. The meridional component (-9.5 ± 15 m s^{-1}) is also within range of the variations of the north-south drift (+15 to −20) obtained at Saint-Santin on March 19, 1974, two solar cycles earlier [*Blanc et al.*, 1977].

The sudden acceleration at 1933 UT (2233 LT) illustrated by Figure 8 may be explained either as a natural phenomena or as an artificial process produced by the HF facility. The average *Kp* for the period of the measurements was 3. Examination of the magnetograms near the Murmansk did not show any magnetic field perturbations near the time of the measured acceleration (A. Ostapenko, private communication, 1995). The rapid change of the drift to near 115 m s^{-1} is unusual but can occur near sunset for a midlatitude ionosphere. For instance, *Blanc et al.* [1977] show a sudden increase in the average zonal drift from 55 to 85 m s^{-1} near 2200 LT with a drop to 35 m s^{-1} 40 min later. This rapid change in motion was connected to the single airglow cloud shown in the last frames of Figures 3 and 6. The artificial irregularities produced by the HF facility may have yielded localized enhancements in electric fields during the 2 min period (1932 to 1934 UT) of this measurement. These enhancements may have been the result of polarization charges accumulated near the ionospheric structures tied to the fast airglow cloud. *Bernhardt et al.* [1988a] have described this charging process.

6. Neutral Winds and Diffusion From O(^1D) Cloud

Remote sensing of the composition in the upper atmosphere has been an active area of research for the past 20 years [*Jacchia*, 1977; *Hedin*, 1987]. Techniques for measuring composition include satellite and rocket mass spectrometry, satellite and rocket extreme ultraviolet (EUV) absorption, incoherent scatter radar analysis, and falling spheres observations [*Hedin*, 1983]. As first suggested by *Bates* [1950], density of neutrals in the upper atmosphere can be determined by the expansion of fluorescent materials released into the thermosphere. Values of the atmospheric diffusion coefficients for sodium and other alkali atoms have been determined from the rate of growth for the diameter of the release [*Rees*, 1961]. By assuming collisional cross sections for the atmospheric species the background neutral density can be determined from the gas cloud diffusion rates.

Similarly, chemical releases have been used to measure neutral winds. Trails of sodium [*Jarrett et al.*, 1963] and trimethyl aluminum [*Mikkelsen and Larsen*, 1993] have provided the neutral wind profiles in the mesosphere and thermosphere. The primary limitation of the chemical release technique is the requirement for a rocket vehicle to deposit the fluorescent material in space. This limitation is eliminated if the fluorescent material can be produced from the ground by high-power radio waves. Figure 1 shows the geometry for generating a glowing cloud using the transmitter at SURA.

The objective of this section is to demonstrate how diffusion coefficients, neutral wind velocities, and collisional quenching times can be determined using artificially excited atomic oxygen O(^1D) as a tracer species. First, high-power radio waves create a steady state cloud of O(^1D) atoms that radiate at 630 nm. Next, the radio wave source is turned off, and the O(^1D) cloud convects and expands according to the local values of neutral winds and diffusion rates. The quenching of O(^1D) by observing artificial 630.0 nm night glow excited by HF transmitters has been previously explored by *Sipler and Biondi* [1972]. They applied their analysis to temporal variations of airglow intensities obtained from a ground-based photometer. Here the analysis uses both temporal and spatial variations from a ground-based imaging system.

The excited species in the artificial airglow cloud can be described with a three-dimensional diffusion equation [*Bernhardt et al.*, 1989a]:

$$\frac{\partial n_1}{\partial t} = \nabla \cdot \left[D_1\left(\nabla n_1 + \frac{n_1}{H_0}\mathbf{z} \right) - \mathbf{v} n_1 \right] - \frac{n_1}{\tau_1} + [\mathrm{O}]R_{01}, \qquad (2)$$

where D_1 is the diffusion coefficient for O(^1D), $H_0 = kT/mg$ is the scale height, k is Boltzmann's constant, T is neutral temperature, m is the oxygen atomic mass, g is the gravitational acceleration, $\mathbf{z}$ is the unit vertical vector, $\mathbf{v}$ is the neutral velocity, τ_1 is the total lifetime of the O(^1D) state, and R_{01} is the excitation rate from accelerated electrons. All of the background parameters (D_1, H_0, and τ_1) are strongly altitude-dependent. The neutral velocity $\mathbf{v}$ is relatively constant over the spatial range of the airglow cloud.

The measured airglow intensity for the red line (630.0 and 636.4 nm) in rayleighs is related to the singlet D density by

$$I = 10^{-6}(A_1 + A_2) \int n_1\, dz, \qquad (3)$$

where $A_1 = 0.00510$ s^{-1} and $A_2 = 0.00164$ s^{-1} are the radiative transition rates from O($^1D_2$) to the O($^3P_2$) and O($^3P_1$) states, respectively. Vertical integration of (2) yields a two-dimensional diffusion-convection equation for the intensity:

$$\frac{\partial I}{\partial t} = D_a\left(\frac{\partial^2 I}{\partial x^2} + \frac{\partial^2 I}{\partial y^2} \right) - v_x \frac{\partial I}{\partial x} - v_y \frac{\partial I}{\partial y} - \frac{I}{\tau_a} + P_a, \qquad (4)$$

where $I(x, y)$ is intensity, D_a is a height-averaged effective diffusion coefficient, v_x and v_y are the horizontal components of the neutral velocity, τ_a is the height-averaged effective lifetime of the O(^1D), including radiation and collisional quenching, and P_a is the airglow source function, which vanishes when the HF is turned off. This equation was derived by *Bernhardt et al.* [1989a] with

$$D_a = \frac{1}{I_1} \int n_1 D_1\, dz, \qquad (5)$$

$$(\tau_a)^{-1} = \frac{1}{I_1} \int \frac{n_1}{\tau_1} dz, \tag{6}$$

$$I_1 = \int n_1 \, dz, \tag{7}$$

$$P_a = 10^{-6}(A_1 + A_2) \int [\mathrm{O}]R_{01} \, dz. \tag{8}$$

Further integration removes the spatial derivatives in (4) by computing the zeroth, first, and second moment with respect to the x and y variables. These moments are defined as

$$\begin{aligned} J(t) &= \int_{-\infty}^{\infty}\int_{-\infty}^{\infty} I(x, y; t) \, dx \, dy; \\ \bar{x}(t) &= \frac{1}{A} \int_{-\infty}^{\infty}\int_{-\infty}^{\infty} xI(x, y; t) \, dx \, dy; \\ \bar{y}(t) &= \frac{1}{A} \int_{-\infty}^{\infty}\int_{-\infty}^{\infty} yI(x, y; t) \, dx \, dy; \\ \overline{x^2}(t) &= \frac{1}{A} \int_{-\infty}^{\infty}\int_{-\infty}^{\infty} x^2I(x, y; t) \, dx \, dy; \\ \overline{y^2}(t) &= \frac{1}{A} \int_{-\infty}^{\infty}\int_{-\infty}^{\infty} y^2I(x, y; t) \, dx \, dy \end{aligned} \tag{9}$$

where t is time. With $P_a = 0$ the parameters τ_1, v_x, v_y, and D_a are obtained from moments of the intensity distribution with the expressions

$$\begin{aligned} \tau_a &= \frac{1}{J}\frac{\partial J}{\partial t}; \qquad v_x = \frac{\partial(\bar{x})}{\partial t}; \qquad v_y = \frac{\partial(\bar{y})}{\partial t}; \\ D_x &= \frac{1}{2}\frac{\partial(\overline{x^2} - \bar{x}^2)}{\partial t}; \qquad D_y = \frac{1}{2}\frac{\partial(\overline{y^2} - \bar{y}^2)}{\partial t}, \end{aligned} \tag{10}$$

where D_x and D_y are independent estimates of D_a for diffusion in the x and y directions, respectively.

The solution to the first equation in (10) and assuming that τ_a is a constant is

$$J(t) = J(0)(1 - \exp[-t/\tau_a]), \tag{11}$$

where the HF pump wave is turned off at $t = 0$. Similar initial value solutions to the other equations in (10) yield expressions for cloud motion

$$\begin{aligned} \bar{x}(t) &= v_x t + \bar{x}(0), \\ \bar{y}(t) &= v_y t + \bar{y}(0), \end{aligned} \tag{12}$$

and diffusive spreading

$$\begin{aligned} \overline{x^2}(t) - \bar{x}(t)^2 &= 2D_a t + \overline{x^2}(0) - \bar{x}(0)^2, \\ \overline{y^2}(t) - \bar{y}(t)^2 &= 2D_a t + \overline{y^2}(0) - \bar{y}(0)^2, \end{aligned} \tag{13}$$

where the initial values at $t = 0$ are based on the cloud conditions when the HF power is turned off.

Since the images are obtained at discrete intervals $\Delta t = 61$ s with integration times $t_0 = 45$ s, the continuous time analysis given by (10) cannot be used. All of the quantities listed in (9) are determined from temporal integration of the intensity variable

$$S_{j+1}(x, y) = \int_{j\Delta t}^{t_0 + j\Delta t} I(x, y; t) \, dt, \tag{14}$$

where $S_j(x, y)$ is the data for image j. Consequently, discrete forms of (10) are used for the analysis. The total integrated intensity in one image is

$$A_j = \iint S_j(x, y) \, dx \, dy = \int_{(j-1)\Delta t}^{(j-1)\Delta t + t_0} J(t) \, dt. \tag{15}$$

Other moments of an image are defined as

$$\begin{aligned} B_{xj} &= \iint xS_j(x, y) \, dx \, dy = \int_{(j-1)\Delta t}^{(j-1)\Delta t + t_0} J(t)\bar{x}(t) \, dt, \\ B_{yj} &= \iint yS_j(x, y) \, dx \, dy = \int_{(j-1)\Delta t}^{(j-1)\Delta t + t_0} J(t)\bar{y}(t) \, dt, \\ C_{xj} &= \iint x^2S_j(x, y) \, dx \, dy = \int_{(j-1)\Delta t}^{(j-1)\Delta t + t_0} J(t)\overline{x^2}(t) \, dt, \\ C_{yj} &= \iint y^2S_j(x, y) \, dx \, dy = \int_{(j-1)\Delta t}^{(j-1)\Delta t + t_0} J(t)\overline{y^2}(t) \, dt. \end{aligned} \tag{16}$$

The integrals over the image act as filters to remove noise fluctuations and extract the bulk properties of the airglow clouds.

Assume that $j = 0$ designates the steady state airglow image and $j = 1$ denotes the image following turnoff of the HF pump wave. From (11) and (15),

$$A_0 = J(0)\Delta t, \tag{17}$$

$$A_1 = A_0(\tau_a/\Delta t)[1 - \exp(-\Delta t/\tau_a)]. \tag{18}$$

With (18), τ_a is determined from the measurements of total integrated image intensity A_0 and A_1. Similarly, using (12) and the first two equations of (16), the horizontal velocities can be obtained from the images with the following equations:

$$v_x = \frac{B_{x1}A_0 - B_{x0}A_1}{A_0(A_1\Delta t + A_1\tau_a - A_0\tau_a)} = \frac{B_{x1}/A_1 - B_{x0}/A_0}{\Delta t + \tau_a(1 - A_0/A_1)}, \tag{19}$$

$$v_y = \frac{B_{y1}A_0 - B_{y0}A_1}{A_0(A_1\Delta t + A_1\tau_a - A_0\tau_a)} = \frac{B_{y1}/A_1 - B_{y0}/A_0}{\Delta t + \tau_a(1 - A_0/A_1)}, \tag{20}$$

where the cloud is assumed to be stationary until the HF wave is turned off and

$$B_{x0} = A_0\bar{x}(0) \qquad B_{y0} = A_0\bar{y}(0). \tag{21}$$

Finally, the cloud expansion is determined from (13) and the last two equations of (16) to give diffusion coefficients D_x and D_y in the x and y directions, respectively. The diffusion coefficients are found from

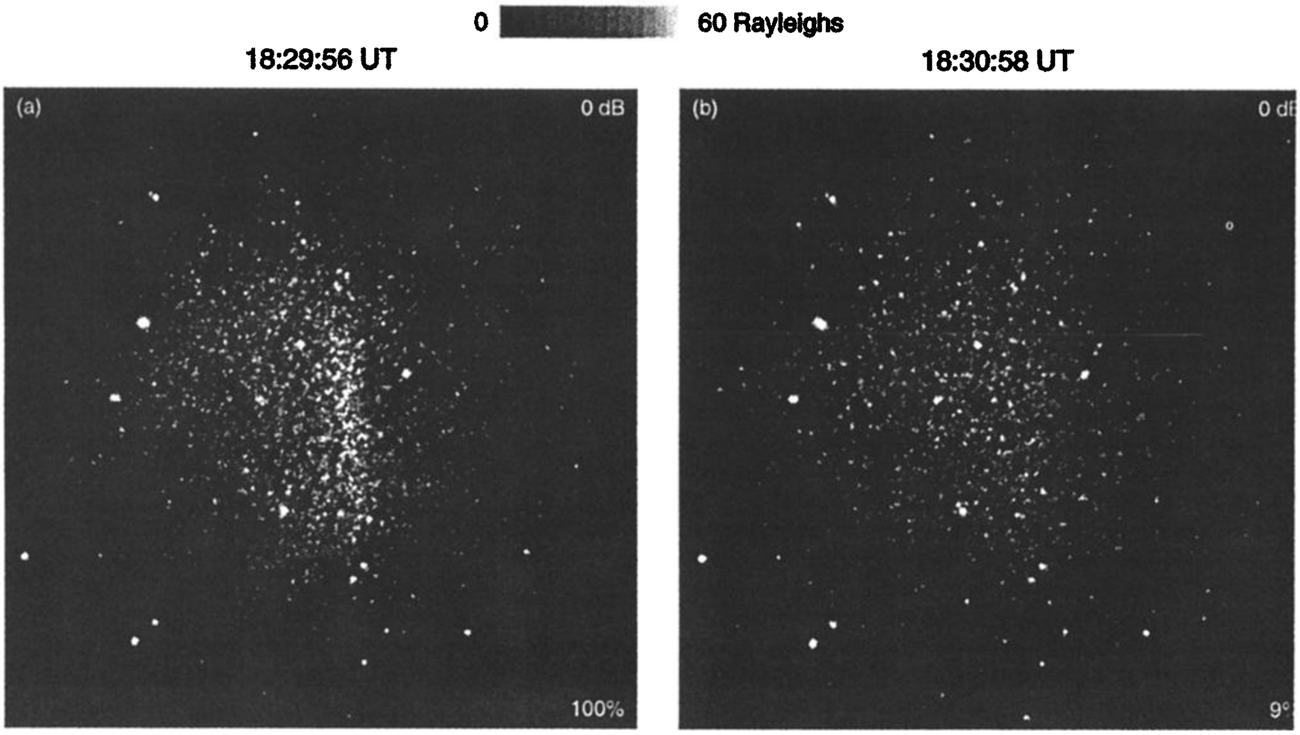

Figure 9. Images taken on March 24, 1995, of (a) a steady state airglow cloud produced by high-power radio waves at 4.3 MHz and (b) a residual cloud that expands and decays after termination of radio waves transmission. Analysis of these two images can yield the lifetime of $O(^1D)$, the horizontal components of neutral wind velocity, and the rate of neutral diffusion in the upper atmosphere.

$$D_x = -\frac{B_{x0}v_x}{A_0} - \frac{v_x^2(\Delta t + \tau_a)}{2} + \frac{C_{x1}A_0 - C_{x0}A_1 + v_x^2\tau_a^2A_0(A_0 - A_1)}{2A_0(A_1\Delta t + A_1\tau_a - A_0\tau_a)}, \tag{22}$$

$$D_y = -\frac{B_{y0}v_y}{A_0} - \frac{v_y^2(\Delta t + \tau_a)}{2} + \frac{C_{y1}A_0 - C_{y0}A_1 + v_y^2\tau_a^2A_0(A_0 - A_1)}{2A_0(A_1\Delta t + A_1\tau_a - A_0\tau_a)}, \tag{23}$$

where the second moment of the steady cloud is given by

$$C_{x0} = A_0\overline{x^2}(0) \qquad C_{y0} = A_0\overline{y^2}(0). \tag{24}$$

Since the horizontal diffusion should be independent of direction, (22) and (23) give independent estimates of $D_a = D_x = D_y$ in the upper atmosphere.

Two sets of data for the diffusion analysis were taken on March 24, 1995, near 1737 and 1830 UT. Figure 9 illustrates the example at 1830 UT where (1) a stable airglow cloud is formed (Figure 9a) and (2) some residual airglow is seen after the HF transmissions have stopped (Figure 9b). The number in the bottom right corner of each image indicates the fraction of the 45 s that the transmitter is on. Since HF was on for 9% in the second image, this fraction of the first image was subtracted from both images and the integration time (Δt) was reduced by 9%. The other image at 1737 UT contained 29% of HF on time and 71% of HF off time. Subtraction of 29% of the HF on image and a 29% reduction of the exposure time was used to compensate for this. After a 5×5 median filter was used to remove stars and speckle noise the diffusion-convection analysis using (15)–(24) was applied to the filtered images.

Measured values of lifetime τ_1, neutral wind velocities v_x and v_y, and diffusion coefficients D_x and D_y were obtained from two artificial airglow clouds produced by HF waves reflecting at 260 and 278 km altitude. The reflection altitudes were determined from analysis of ionograms obtained with an ionosonde located at the SURA HF site. The reflection altitude is taken to be the true height on the plasma density profile where the HF transmitter frequency equals the F region plasma frequency. When the transmitter frequency was 4.785 MHz, the reflection altitude was 278 km. When the transmitter was reduced to 4.3 MHz, the reflection altitude dropped to 260 km.

Image processing of the 630 nm intensities yields the results given in Table 2. A comparison between the estimated values of diffusion coefficient shows that $D_x \cong D_y$ and that the diffusion coefficient increases with source altitude. Also, the lifetime of the $O(^1D)$ state is greater for a 278 km source altitude than for a 260 km altitude. Both these effects are the consequence of lower neutral densities at higher altitudes. A more quantitative evaluation of the results, using an empirical model for neutral densities and winds, is given in section 7.

7. Comparison With Model Neutral Winds and Diffusion Coefficients

The results of the HPAA analysis will be compared with neutral atmospheric parameters determined using the Mass

Table 2. Artificial $O(^1D)$ Cloud Analysis Compared With Mass Spectrometer Incoherent Scatter (MSIS-86) Model on March 24, 1995

	1829:56 UT at 260 km Altitude		1736:45 UT at 278 km Altitude	
	Measured Value	Modeled Value	Measured Value	Modeled Value
D_x, cm^2 s^{-1}	1.36×10^{11}		2.83×10^{11}	
D_a, cm^2 s^{-1}		1.96×10^{10}		2.81×10^{10}
D_y, cm^2 s^{-1}	8.04×10^{10}		2.94×10^{11}	
τ_a, s	29.4	42.4	43.4	53.1

Spectrometer Incoherent Scatter (MSIS-86) model [*Hedin*, 1987]. The thermospheric densities and pressure gradients obtained from MSIS-86 are used to generate $O(^1D)$ lifetimes, neutral winds, and diffusion rates.

The theoretical value of lifetime (τ_1) is

$$\tau_1 = (A_{1D} + k_1[N_2] + k_2[O_2] + k_3[e-] + k_4[O])^{-1}, \qquad (25)$$

where the constants $A_{1D} = 9.34 \times 10^{-3}$, $k_1 = 2.0 \times 10^{-11} \exp(107.8/T_n)$ cm^3 s^{-1}, $k_2 = 2.9 \times 10^{-11} \exp(67.5/T_n)$ cm^3 s^{-1}, $k_3 = 6.6 \times 10^{-10}$ cm^3 s^{-1}, and $k_4 = 8 \times 10^{-12}$ cm^3 s^{-1} are given by *Sobral et al.* [1993] and *Melendez-Alvira et al.* [1995].

The theoretical value for the diffusion coefficient is obtained from the binary diffusion for $O(^1D)$ through each of the neutral species in the atmosphere. The total diffusion coefficient (D_0) is the reciprocal sum of the individual diffusion coefficients according to

$$D_0 = \left(\sum_j D_j^{-1} \right)^{-1}, \qquad (26)$$

where $D_j = A_j T^{s_j}/nj$. A_j and s_j are constants from *Yee and Dalgarno* [1987] for diffusion in O and from *Banks and Kockarts* [1973] for diffusion in molecular species (O_2 and N_2), and n_j is the density of species "j". The constants, densities, model diffusion coefficients, and lifetimes for $O(^1D)$ are given in Table 2 for the two altitudes of the measurements. Model profiles for the diffusion coefficient and $O(^1D)$ lifetime are given in Figure 10.

The measured quantities τ_a, v_x, v_y, and $D_a = D_x = D_y$ are weighted by the profiles for the excited state according to (5) and (6). The $O(^1D)$ profiles are calculated using the numerical model of energetic electron transport, collisional excitation, and diffusion transport given by *Bernhardt et al.* [1989a]. A suprathermal source with 0.001% of the ambient electrons in a Maxwellian distribution having a characteristic energy of 1.72 eV yields the measured intensities of 630 nm airglow. This source at 260 km altitude gives the profiles of excited atomic oxygen illustrated in Figure 11. With this $O(^1D)$ profile and the computed values diffusion and quenching rates in Figure 10, equations (5) and (6) are used to provide the weighted average values of diffusion coefficients $O(^1D)$ lifetimes that are given in Table 3.

The following differences between the measured parameters and the model parameters are noted. The measured diffusion coefficients are consistently a factor of 10 larger than those provided by the model. The measured diffusion coefficient is consistent with a region ~80 km above the source altitude. The airglow cloud diffuses more rapidly at higher altitudes, and estimates based on cloud expansion may be biased toward higher altitudes. The measured $O(^1D)$ lifetimes are consistently shorter than those provided by the model. The measured lifetime is representative of a region 25 km below the source altitude. The more rapid quenching of the airglow cloud at lower altitudes may provide this difference.

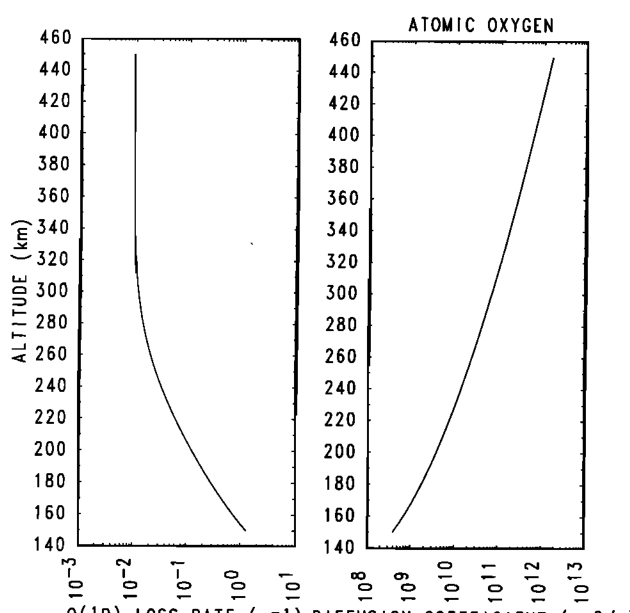

Figure 10. Total loss rate and diffusion coefficient for $O(^1D)$ in the Mass Spectrometer Incoherent Scatter (MSIS-86) model atmosphere.

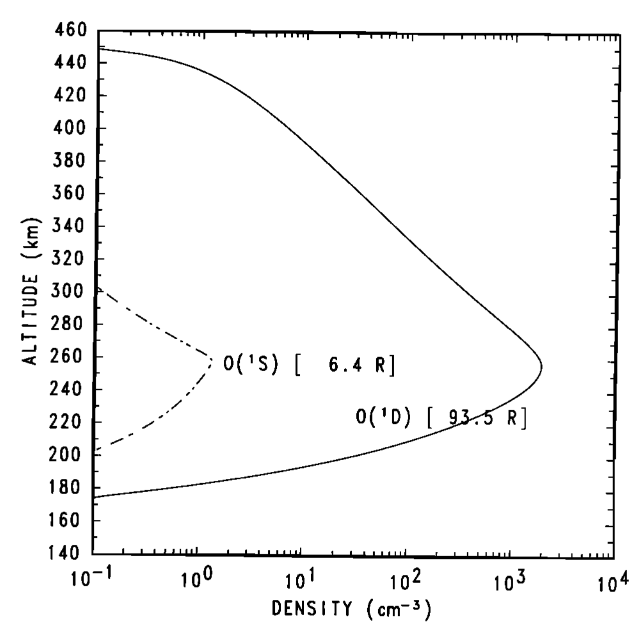

Figure 11. Computed profiles of $O(^1D)$ and $O(^1S)$ excited by high-power radio waves reflecting at 260 km altitude. The red line intensity is 93.5 R. Rapid vertical diffusion of $O(^1D)$ on the topside of the airglow layer yields a scale height of 24.7 km. The $O(^1D)$ density falls off more rapidly on the bottomside of the airglow cloud.

Table 3. MSIS-86 Model Based Diffusion Coefficients and Radiative Lifetime for $O(^1D)$

	Species				Comments	
	O	O_2	N_2	Total	H, km	T, K
A_j	2.06×10^{17}	9.69×10^{16}	9.69×10^{16}			
s_j	0.615	0.774	0.841			
n_j at 1830 UT, cm^{-3}	8.0×10^8	1.0×10^7	2.5×10^8	$n = 1.06 \times 10^9$	260	822
D_j, $cm^2\ s^{-1}$	1.60×10^{10}	1.75×10^{12}	1.10×10^{11}	$D_0 = 1.38 \times 10^{10}$	260	822
$k_j n_j$	6.4×10^{-3}	0.3×10^{-3}	5.7×10^{-3}	$\tau_1 = 46.1$	260	822
n_j at 1737 UT, cm^{-3}	4.0×10^8	4.0×10^6	1.2×10^8	$n = 5.24 \times 10^8$	278	830
D_j, $cm^2\ s^{-1}$	3.21×10^{10}	4.40×10^{13}	2.30×10^{11}	$D_0 = 2.82 \times 10^{10}$	278	830
$k_j n_j$	3.2×10^{-3}	0.1×10^{-3}	2.7×10^{-3}	$\tau_1 = 65.1$	278	830

The results of the neutral wind components extracted from the March 1995 data and the plasma drifts obtained during the same period 2 years earlier are summarized in Table 4. These horizontal velocities are compared with neutral winds derived using the horizontal wind model 1990 (HWM90) [*Hedin et al.*, 1991] and plasma drifts measured at Saint-Santin in March 1974. The measured neutral winds determined from the artificial airglow source show reasonable agreement with the HWM90 model. The measured meridional east-west wind is a good match with the model value. The zonal northward component is larger than that provided by HWM90 but is in the same direction. The neutral wind drives the quiet ionospheric wind dynamo in the E region to produce electric fields that induce $\mathbf{E} \times \mathbf{B}$ drifts in the F region [*Salah and Holt*, 1974]. If the E region Pedersen conductivities at night become small compared to the F region Pedersen conductivities, the F region can become polarized to produce $\mathbf{E} \times \mathbf{B}$ drifts in the direction of the neutral wind. Consequently, it is not surprising that the zonal neutral wind speed (96 m s^{-1}) in Table 4 is of the same order as the $\mathbf{E} \times \mathbf{B}$ drift speed (70 m s^{-1}) measured during the same time period 2 years earlier at SURA. Simultaneous and independent measurements of the neutral winds and plasma drifts can provide information on the electrostatic interactions in the ionosphere.

8. Conclusions and Future Work

Remote sensing of the upper atmosphere with HPAA clouds produced over the HF facility at SURA, Russia, has been presented here for the equinox periods of March 1993 and 1995. Images of the airglow clouds have been used (1) to demonstrate F region layer penetration by the HF beam, (2) to illustrate the importance of phasing the HF antenna for forming and pointing the radio beam, (3) to determine thresholds for acceleration of electrons, (4) to measure plasma drifts with high temporal resolution, and (5) to provide quenching rates, winds, and diffusion coefficients in the neutral atmosphere. The methods for image processing of the airglow clouds to provide atmospheric quantities have included (1) filtering to remove noise and point sources, (2) performing cross correlations, and (3) finding integral moments of image intensities.

The results presented here could be improved with increased airglow intensities and lower noise imaging systems. Figure 9, for example, shows the effects of scintillations and photo counting noise. The intensity of the airglow is determined by the capabilities of the HF facilities including transmitter power, antenna gain, and beam width. Most HF facilities are able to produce red line airglow from F region heating with maximum intensities in the 100–200 R range by using effective radiated powers (ERP) of the order of 100–250 MW. The higher power facilities such as the "super heater" in Tromsö, which has an ERP of 1200 MW, and the High Frequency Active Auroral Research Project (HAARP) facility in Alaska, which has a design ERP of 1600 MW, should be able to produce higher intensities. Attempts to increase the airglow intensities with pulsing or electron gyro heating were not successful.

The data presented here used an intensified, cooled CCD camera. The intensifier with a gain of 1000 is used to produce an optical flux on the CCD that is larger than the detector readout noise. Consequently, the optical data are dominated by intensifier noise. An alternative imaging system using a bare, cooled CCD could be employed for improved image quality if the detector readout noise is low enough. Other sources of noise in the image data include stars, scattered sunlight at dawn and dusk, moonlight, and meteorological obscurants.

A fundamental limitation of the HPAA measurements is that at night the ionospheric densities decay to the point that the HF waves are no longer reflected. The lowest transmission frequency varies with facility: 2.8 MHz at the HAARP and High-Power Auroral Stimulation (HIPAS) facilities in Alaska; 3.175 MHz at Arecibo; 3.85 MHz at the EISCAT heating facility in Tromsö; 4.3 MHz at SURA, Russia; and 5.5 MHz at the EISCAT super heater in Tromsö. The corresponding min-

Table 4. Data Comparison of Artificial Red-line Cloud Analyzed for Winds and Drifts

	March 24, 1995 at 1830 UT		March 21, 1993 at 1930 UT	
	Measured Neutral Wind	Modeled Neutral Wind*	Measured Plasma Drift	March 19, 1974 ISR Drifts
Zonal Component, m s^{-1}	96.0	25.2	68.0	35 to 95
Meridional Component, m s^{-1}	−68.6	−77.6	−9.5	+15 to −20

*Horizontal wind model 1990.

imum densities for reflection in the F region fall in the range of 9.7×10^4 to 3.7×10^5 cm^{-3}, depending on facility. The nighttime values of peak F region density often fall below these values, especially at solar minimum. The most useful facility for nighttime airglow studies has the capability of transmitting below the critical frequencies of the F layer throughout the night.

HF pumped artificial airglow (HPAA) can be a powerful tool to study the upper atmosphere. Future experiments should employ the steering capabilities of the antenna arrays to excite emissions over horizontal ranges of a few hundred kilometers at F region altitudes. Modern HF facilities and improved imaging systems can be used together for novel studies of the thermosphere using the HPAA technique described here.

Acknowledgments. The authors are indebted to the staff of the Radiophysical Research Institute (NRIFI) of Nizhny Novgorod, Russia, for their support during the optical observations campaign. We are particularly indebted to V. V. Bychkov, A. N. Karashtin, Y. A. Shlugaev, G. P. Komrakov, and the engineering staff at the SURA HF facility for making the measurements possible. The Office of Naval Research supported the work at the Naval Research Laboratory. This research was conducted while M. Wong was participating in the Science and Engineering Apprenticeship Program at NRL.

Janet G. Luhmann thanks Peter Stubbe and another referee for their assistance in evaluating this paper.

References

Adieshvili, T. B., et al., Ionospheric emission caused by an intense radio wave, *Sov. J. Plasma Phys.*, Engl. Transl., *4*, 721–726, 1978.

Banks, P. M., and G. Kocharts, *Aeronomy, Part A*, Academic, San Diego, Calif., 1973.

Bates, D. R., A suggestion regarding the use of rockets to vary the amount of atmospheric sodium, *J. Geophys. Res.*, *55*, 347–349, 1950.

Belikovich, V. V., E. A. Benediktov, G. G. Getmantsev, Y. A. Ignat'ev, and G. P. Komrakov, Scattering of radio waves form the artificially perturbed F region of the ionosphere, *JETP Lett.*, Engl. Transl., *22*, 243–244, 1975.

Bernhardt, P. A., L. M. Duncan, and C. A. Tepley, Artificial airglow excited by high-power radio waves, *Science*, *242*, 1022–1027, 1988a.

Bernhardt, P. A., L. M. Duncan, C. A. Tepley, R. A. Behnke, and J. P. Sheerin, Spatial and temporal evolution of 630.0 nm airglow enhancements during ionospheric heating experiments, *Adv. Space Res.*, *8*(1), 271–277, 1988b.

Bernhardt, P. A., L. M. Duncan, and C. A. Tepley, Heater-induced cavities as optical tracers of plasma drifts, *J. Geophys. Res.*, *94*, 7003–7010, 1989a.

Bernhardt, P. A., C. A. Tepley, and L. M. Duncan, Airglow enhancements associated with plasma cavities formed during ionospheric heating experiments, *J. Geophys. Res.*, *94*, 9071–9092, 1989b.

Bernhardt, P. A., W. A. Scales, S. M. Grach, A. N. Karashtin, D. S. Kotik, and S. V. Polyakov, Excitation of artificial airglow by high power radio waves from the "SURA" ionospheric heating facility, *Geophys. Res. Lett.*, *18*, 1477–1480, 1991.

Bernhardt, P. A., L. S. Wagner, J. A. Goldstein, V. Y. Trakhtengerts, E. N. Ermakova, V. O. Rapoport, P. Komrakov, and A. M. Babichenko, Enhancement of stimulated electromagnetic emission during two frequency ionospheric heating experiments, *Phys. Rev. Lett.*, *72*, 2879–2882, 1994.

Bernhardt, P. A., et al., The ionospheric focused heating experiment, *J. Geophys. Res.*, *100*, 17,331–17,345, 1995.

Blanc, M., and P. Amayenc, Seasonal variations of the ionospheric $E \times B$ drifts above Saint-Santin on quiet days, *J. Geophys. Res.*, *84*, 2691–2704, 1979.

Blanc, M., P. Amayenc, P. Bauer, and C. Taieb, Electric field induced drifts from the French incoherent scatter facility, *J. Geophys. Res.*, *82*, 87–97, 1977.

Bracewell, R. N., *Two-Dimensional Imaging*, Prentice-Hall, Englewood Cliffs, N. J., 1995.

Brändström, B. U. E., T. B. Leyser, Å. Steen, M. T. Rietveld, B. Gustavsson, T. Aso, and M. Ejiri, Unambiguous evidence of HF pump-enhanced airglow at auroral latitudes, *Geophys. Res. Lett.*, *26*, 3561–3564, 1999.

Carlson, H. C., V. B. Wickwar, and G. P. Mantas, Observations of fluxes of suprathermal electrons accelerated by HF excited instabilities, *J. Atmos. Terr. Phys.*, *44*, 1089–1100, 1982.

Djuth, F. T., K. M. Groves, J. H. Elder, E. R. Shinn, J. M. Quinn, J. Villasenor, and A. Y. Wong, Measurements of artificial periodic inhomogeneities at HIPAS Observatory, *J. Geophys. Res.*, *102*, 24,023–24,035, 1997.

Fejer, J. A., C. A. Gonzales, H. M. Ierkic, M. P. Sulzer, C. A. Tepley, L. M. Duncan, and F. T. Djuth, Ionospheric modification experiments with the Arecibo heating facility, *J. Atmos. Terr. Phys.*, *47*, 1165–1179, 1985.

Gurevich, A. V., and G. M. Milikh, Artificial airglow due to modifications of the ionosphere by powerful radio waves, *J. Geophys. Res.*, *102*, 389–394, 1997.

Gurevich, A. V., T. Hagfors, H. Carlson, A. V. Lukyanov, and K. P. Zybin, Electron temperature measurements by incoherent scattering in the presence of strong small scale temperature irregularities, *Phys. Lett. A*, *246*, 335–340, 1998.

Hansen, J. D., G. J. Morales, and J. E. Maggs, Large-scale HF-induced ionospheric modifications: Theory and modeling, *J. Geophys. Res.*, *97*, 17,019–17,032, 1992.

Haslet, J. C., and L. R. Megill, A model of the enhance airglow excited by RF radiation, *Radio Sci.*, *9*, 1005–1019, 1974.

Hedin, A. E., A revised thermospheric model based on mass spectrometer and incoherent scatter data: MSIS-83, *J. Geophys. Res.*, *88*, 10,170–10,188, 1983.

Hedin, A. E., MSIS-86 thermospheric model, *J. Geophys. Res.*, *92*, 4649–4662, 1987.

Hedin, A. E., et al., Revised global model of thermosphere winds using satellite and ground-based observations, *J. Geophys. Res.*, *96*, 7657–7688, 1991.

Henriksen, K., W. Stoffregen, B. Lybekk, and A. Steen, Photometer and spectrometer seach of the oxygen green and redlines during artificial ionospheric heating in the auroral zone, *Ann. Geophys.*, *2*, 73–76, 1984.

Huang, J., and S. P. Kuo, A theoretical model for the broad upshifted maximum in the stimulated electromagnetic emission spectrum, *J. Geophys. Res.*, *99*, 19,569–19,576, 1994.

Hussein, A. A., W. A. Scales, and J. Huang, Theoretical and simulation studies of broad upshifted sideband generation in ionospheric stimulated radiation, *Geophys. Res. Lett.*, *25*, 955–958, 1998.

Jacchia, L. G., Thermospheric temperature, density, and composition, in *New Models*, *Spec. Rep. 357*, Smithson. Astrophys. Obs., Cambridge, Mass., 1977.

Jarrett, A. H., G. J. McGratten, and J. A. Rees, The measurement of high altitude wind velocities from vapour releases, I, *Planet. Space Sci.*, *11*, 1309–1310, 1963.

Kelley, M. C., T. L. Arce, J. Salowey, M. Sulzer, W. T. Armstrong, M. Carter, and L. M. Duncan, Density depletions at the 10-m scale induced by the Arecibo heater, *J. Geophys. Res.*, *100*, 17,367–17,376, 1995.

Leyser, T. B., B. Thide, H. Derblom, A. Hedberg, B. Lundborg, P. Stubbe, and H. Kopka, Stimulated electromagnetic emission near electron cyclotron harmonics in the ionosphere, *Phys. Rev. Lett.*, *63*, 1145–1147, 1989.

Mantas, G. P., Large 6300-Å airglow intensity enhancements observed in ionosphere heating experiments are excited by thermol electrons, *J. Geophys. Res.*, *99*, 8993–9002, 1994.

Mantas, G. P., and H. C. Carlson, Reinterpretation of the 6300-Å airglow enhancements observed in ionosphere heating experiments based on analysis of Platteville, Colorado, data, *J. Geophys. Res.*, *101*, 195–209, 1996.

Melendez-Alvira, D. J., D. G. Torr, P. G. Richards, W. R. Swift, M. R. Torr, T. Baldridge, and H. Rassoul, Sensitivity of the 6300 Å twilight airglow to neutral composition, *J. Geophys. Res.*, *100*, 7839–7853, 1995.

Mikkelsen, I. S., and M. F. Larsen, Comparison of spectral thermospheric general circulation model simulations and E and F region chemical release wind observations, *J. Geophys. Res.*, *98*, 3693–3709, 1993.

Moore, J. G., Airglow morphology during an ionospheric heating experiment at Platteville, Colorado, *AFGL Tech. Rep.*, *AFTL-TR-83-0238*, 1983.

Rees, J. A., Diffusion coefficients determined from sodium vapour trails, *Planet. Space Sci.*, *8*, 35–42, 1961.

Rietveld, M. T., E. Turunen, H. Matveinen, N. P. Goncharov, and P. Pollari, Artificial periodic irregularities in the auroral ionosphere, *Ann. Geophys.*, *14*, 1437–1453, 1996.

Salah, J. E., and J. M. Holt, Midlatitude thermospheric winds from ioncoherent scatter radar and theory, *Radio Sci.*, *9*, 301–313, 1974.

Sergienko, T., I. Kornilov, E. Belova, T. Turunen, and J. Mannin, Optical effects in the aurora caused by ionospheric HF heating, *J. Atmos. Sol. Terr. Phys.*, *59*, 2401–2407, 1997.

Sipler, D. P., and M. A. Biondi, Measurements of $O(^1D)$ quenching rates in the *F* region, *J. Geophys. Res.*, *77*, 6202–6212, 1972.

Sobral, J. H. A., H. Takahashi, M. A. Abdu, P. Muralikrishna, Y. Sahai, C. J. Zamultti, E. R. de Paula, and P. P. Batista, Determination of the quenching rate of the $O(^1D)$ by $O(^3P)$ from rocket-borne optical (630 nm) and electron density data, *J. Geophys. Res.*, *98*, 7791–7798, 1993.

Stubbe, P., Review of ionospheric modification experiments at Tromsö, *J. Atmos. Terr. Phys.*, *58*, 349–368, 1996.

Stubbe, P., et al., Ionospheric modification experiment in northern Scandinavia, *J. Atmos. Terr. Phys.*, *44*, 1025–1041, 1982.

Stubbe, P., A. J. Stocker, F. Honary, T. R. Robinson, and T. B. Jones, Stimulated electromagnetic emissions (SEE) and anomalous FH wave absorption near electron gyroharmonics, *J. Geophys. Res.*, *99*, 6233–6246, 1994.

Utlaut, W. F., and R. Cohen, Modifying the ionosphere with intense radio waves, *Science*, *174*, 245–254, 1971.

Wagner, L. S., P. A. Bernhardt, J. A. Goldstein, C. A. Selcher, V. L. Frolov, and E. N. Sergeev, The effect of ionospheric self- and pre-conditioning on the broad upshifted maximum (BUM), *J. Geophys. Res.*, *104*, 2573–2590, 1999.

Wang, J. G., D. L. Newman, and M. V. Goldman, Vlasov simulations of electron heating by langmuir turbulence near the critical altitude in the radiation modified ionosphere, *J. Atmos. Sol. Terr. Phys.*, *59*, 2461–2474, 1997.

Yee, J.-H., and A. Dalgarno, Energy transfer of $O(^1D)$ atoms in collision with $O(^3P)$ atoms, *Planet. Space Sci.*, *35*, 399–404, 1987.

P. A. Bernhardt, Beam Physics Branch, Plasma Physics Division, Naval Research Laboratory, Code 6794, 4555 Overlook Avenue, S. W., Washington, DC 20375-5320. (bern@ppd.nrl.navy.mil)

B. G. Fejer, Center for Atmospheric and Space Sciences, 246 SER Building, Utah State University, Logan, UT 84322-4405. (bfejer@cc.usu.edu)

V. L. Frolov and E. N. Sergeev, Radiophysical Research Institute, 603600 Nizhny Novgorod, Russia. (vf@nirfi.sci.nnov.ru)

J. A. Goldstein, C. A. Selcher, and L. S. Wagner, Information Technology Division, Code 5554, Naval Research Laboratory, Washington, DC 20375-5337. (wagner@itd.nrl.navy.mil)

J. D. Huba, Beam Physics Branch, Plasma Physics Division, Naval Research Laboratory, Code 6790, 4555 Overlook Avenue, S. W., Washington, DC 20375-5320. (huba@ppdhuba.nrl.navy.mil)

M. Wong, Department of Physics, Carnegie Mellon University, Pittsburgh, PA 15213.

(Received September 29, 1999; revised January 7, 2000; accepted January 7, 2000.)